Chemical Engineering Journal 512 (2025) 162226

Contents lists available at ScienceDirect

Chemical Engineering Journal

journal homepage: www.elsevier.com/locate/cej

Tuning the acid-base properties of layered double hydroxides for the selective obtention of cyclohexane and cyclohexanol in the hydrodeoxygenation of guaiacol

Angie C. Rueda [a], Judith Granados-Reyes [a], Julien Delaunay [a], Pau Mora-Masià [a], Yolanda Cesteros [a,*]

[a] Universitat Rovira i Vigili, Departament de Química Física i Inorgànica, C/ Marcel·lí Domingo, 1 43007 Tarragona, Spain

ARTICLE INFO

Keywords:
Hydrodeoxygenation
Guaiacol
Layered double hydroxides
Cyclohexane
Cyclohexanol

ABSTRACT

Ni and NiCu catalysts were prepared from Ni/Al, Ni/Cu/Al, Ni/MgAl, and Ni/Cu/Mg/Al hydrotalcites (HT) and tested for the hydrodeoxygenation of guaiacol, a lignin model compound, under H_2 pressure at 300 °C to obtain the added-value products cyclohexane and cyclohexanol. The catalysts prepared from HT without magnesium were more selective to cyclohexane (48–65 %) than those prepared from HT with magnesium, which obtained higher selectivity to cyclohexanol (46–72 %). The presence of magnesium oxide species decreased the reducibility and the metallic area of the catalysts, decreased the Ni content in the NiCu alloy formed in the bimetallic catalyst, and, due to their higher basicity, inhibited the dehydration of cyclohexanol, a key step for obtaining cyclohexane. The obtention of cyclohexane with catalysts prepared from HT is remarkable and could be mainly explained by the reaction temperature used (300 °C) since when it was lowered to 240 °C, a significant decrease of cyclohexane accompanied by an increase of cyclohexanol was observed. When these catalysts were combined with H-βeta, the additional Brønsted acidity led to the overproduction of cyclohexane due to the parallel transformation of the solvent used, dodecane, under the reaction conditions. The detection of some amounts of benzene and toluene suggested a different reaction pathway compared with the catalysts without H-βeta. Finally, the addition of small amounts of Lewis acidity (ReOx) to the Ni/Al and NiCu/Al catalytic systems made difficult the reducibility to Ni of their catalytic precursors and promoted the binding of the oxygenated compounds, favoring the formation of cyclohexanol.

1. Introduction

As the population continues to grow, so do energy-demanding processes. Although renewable energy sources have expanded in the past few years, accounting for 8.2 % of global primary energy in 2024 (excluding hydroelectric energy), fossil fuels still provide over 81.5 % of global primary energy, increasing CO_2 emissions, according to the Energy Institute (EI) [1]. European Union (EU) has progressively promoted initiatives to reduce the dependence on fossil fuels by integrating renewable energy sources, such as biofuels, into its energy mix [2]. However, most biofuels production relies on food crops competing with the food sector. Considering that EU policies target to increase the share of renewable energy by at least 42.5 % by 2030 [3], an interesting alternative remains for obtaining biofuels from lignocellulosic biomass derived from agriculture or forestry wastes [4].

Lignocellulosic biomass contains lignin, a polyaromatic molecule with high carbon-to-oxygen ratio, which makes it a promising building block biofuels source [5]. There are several approaches for the conversion of lignin into biofuels, which include the catalytic hydrodeoxygenation (HDO) of lignin-derived bio-oils previously obtained from pyrolysis or liquefaction of biomass [6,7], and the direct catalytic HDO of lignin, previously extracted from biomass [8,9]. However, its depolymerization remains difficult due to its structure complexity. Thus, model compound molecules, such as guaiacol, cresol, and catechol, have been used to study the C-O and C-C cleavage to obtain low-oxygenated molecules, appropriate for transportation fuels [7].

Hydrodeoxygenation of guaiacol has been widely studied at temperatures higher than 200 °C under H_2 pressure with different catalytic systems [10–19]. Scheme 1 shows the main pathways proposed in the literature for the HDO of guaiacol in these reaction conditions. [6,20–24].

* Corresponding author.
E-mail address: yolanda.cesteros@urv.cat (Y. Cesteros).

https://doi.org/10.1016/j.cej.2025.162226
Received 13 January 2025; Received in revised form 19 March 2025; Accepted 31 March 2025
Available online 3 April 2025

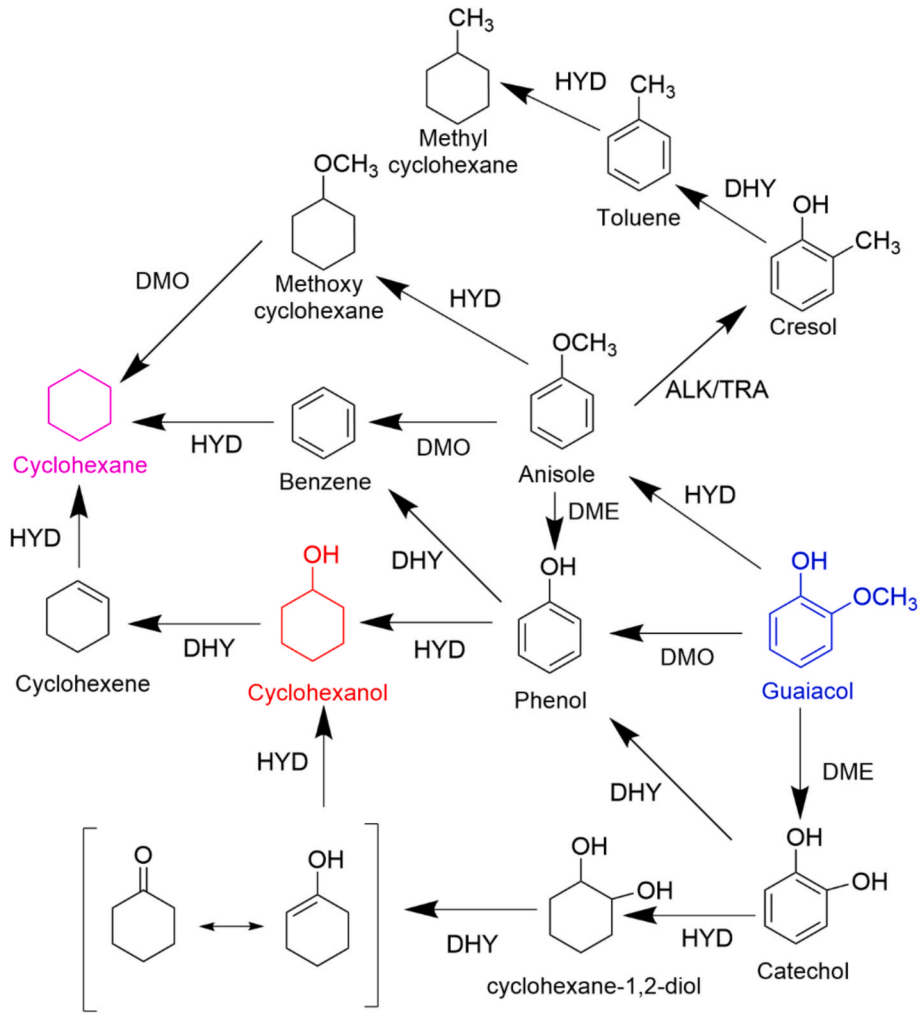

Scheme 1. Guaiacol hydrodeoxygenation pathways at reaction temperatures higher than 200 °C. DM: Demethylation, DMO: Demethoxylation, HYD: Hydrogenation, DHY: Dehydration, ALK/TRA: Transalkylation.

Several authors used noble metals for the HDO of guaiacol due to their high affinity to hydrogen, good dispersion, and lower deactivation allowing high hydrogenation activity. Lee et al. [14,25] studied this reaction with Pt/H-zeolites at 250 °C and 40 bar of H_2, obtaining cyclohexane as the main product with 45 % selectivity for a 95 % conversion with Pt/HBeta and 70 % selectivity for a low conversion (~22 %) with Pt/HY. Shu et al. [15] reported a selectivity towards cyclohexane of almost 100 % for a practically total conversion when using Ru/TiO_2-CeO_2 at 230 °C with 10 bar of H_2 for 4 h. However, the high cost and scarcity of noble metals limit their applications.

Cheaper transition metals, like Ni, Fe, and Co, alone or combined, have also been tested for guaiacol hydrodeoxygenation. Blanco et al. [10] studied the synergy between Ni and Co nanoparticles supported on carbon at 300 °C and 50 bars of H_2 obtaining phenol, cresol, cyclohexanol, and methylanisole depending on the Ni:Co ratio. Recently, Matos et al. [16] reported the use of Ni-Ca/active carbon (AC) and Ni-Mg/active carbon as catalysts for the HDO of guaiacol at 300 °C under 50 bar of H_2 for 4 h. Cyclohexane was obtained in high amounts (98.9 % of selectivity) with Ni-Mg(5 %)/AC while phenol was the main product (72.6 % of selectivity) with Ni-Ca(5 %)/AC for a total conversion. Furthermore, Liu et al. [17] studied this reaction at 300 °C with 40 bar of H_2 for a longer time, 8 h, using a $Cu\text{-}ZnO\text{-}Al_2O_3$ catalyst obtaining 81.3 % yield of cyclohexane with methylcyclohexane, bicyclohexyl and benzene in lower amounts.

Supported metal catalysts derived from hydrotalcite-like materials, which are a type of layered double hydroxides (LDHs) with chemical formula $M^{2+}_{1-x}M^{3+}_{x}(OH)_2A^{n-}_{x/n}{\cdot}yH_2O$, have shown great potential in hydrogenations reactions. In these materials, divalent (M^{2+}) and trivalent (M^{3+}) cations form positive charged layers, which are balanced by interlamellar anions (A^{n-}). Additionally, their acid-base properties can be tailored since elements, such as Ni, Cu and Co can be used as divalent cations along with the classic Mg and Al, obtaining mixed oxides after calcination and well dispersed supported metallic catalysts after reduction [26–28]. There are few studies of HDO of guaiacol with catalysts obtained from LDHs [29–32]. Guo et al. [29] prepared NiCo/AlOx catalyst from NiCoAl LDH and obtained 90 % selectivity to cyclohexanol for a total conversion of guaiacol when the HDO was tested at 180 °C under 20 bar of H_2 for 1 h. Moreover, the presence of basic centers has been reported to suppress the dehydration step, particularly Ni-Fe/MgAlOx catalysts prepared from NiFeMgAl hydrotalcites, led to high yield of cyclohexanol (96 %) at 200 °C, 30 bar H_2 for 2.5 h [30]. Whang et al. [31] reported 88 % selectivity towards cyclohexanol using a Ru/ZnAlPWO derived from phosphotungstate intercalated ZnAl LDH precursor at 250 °C with 20 bar of H_2. Perez et al. [32] used Ni and Co hydrotalcite-based catalysts at 350 °C under 70 bar of H_2 for 4 h. The Ni-based catalyst produced 1-methyl-1,2-cyclohexanediol as main product (70 %) while Co-based catalyst led cyclohexanol (41 %).

Both cyclohexanol and cyclohexane, valuable products of guaiacol HDO, are targeted industrial products. Cyclohexane can be used as a nonpolar solvent for lacquers, resins, and fats [33] and as a component

Table 1
Theoretical composition of the LDHs prepared.

Samples	Ni/Almolar ratio	Cu/Almolar ratio	Mg/Almolar ratio	M^{2+}/M^{3+}molar ratio
HT_{NiAl}	3.0	–	–	3.0
HT_{NiMgAl}	2.0	–	1.0	3.0
HT_{NiCuAl}	1.5	1.5	–	3.0
$HT_{NiCuMgAl}$	1.0	1.0	1.0	3.0

in diesel and biodiesel fuel blends considering its high octane number (~83). The addition of cyclohexane shortens the ignition delay time of fuels prolonging combustion and reducing NO emissions in the engine [34]. Cyclohexane and cyclohexanol can also be converted into adipic acid, which is a precursor of nylon 6,6 and polyurethanes [35–38].

This study aimed to synthesize and characterize Ni and Ni-Cu catalysts derived from NiAl, NiCuAl, NiMgAl, and NiCuMgAl LDHs to evaluate the effect of the precursor composition on the selective obtention of cyclohexane and cyclohexanol for the hydrodeoxygenation of guaiacol at 300 °C under H_2. Up to now, cyclohexane has not been reported with catalysts obtained from hydrotalcite-type materials. Special attention will be paid to study the effect of adding Brønsted and Lewis acidity to these catalytic systems on the catalytic activity.

2. Experimental

2.1. Materials

$Ni(NO_3)_2{\cdot}6H_2O$ (Scharlau, 98 %), $Cu(NO_3)_2{\cdot}3H_2O$ (Scharlau, 98 %), $Al(NO_3)_3{\cdot}9H_2O$ (Scharlau, 98 %), and $Mg(NO_3)_2{\cdot}6H_2O$ (Charla, 98 %), $Na_2CO_3{\cdot}10H_2O$ (Scharlau, 98 %), NaOH solution (Sigma-Aldrich, 98 %), NH_4ReO_4 (≥99 % from Alfa Aesar) Guaiacol (≥ 98 %, Alfa Aesar Chemicals), n-dodecane (99 %, Thermo Fisher Scientific) and hexadecane (99 %, Alfa Aesar Chemicals) were purchased and used without further purifications.

2.2. Preparation of catalytic precursors

Layered double hydroxides containing Ni, Cu, Mg, and Al, with an M^{2+}/M^{3+} ratio of 3 were synthesized via traditional co-precipitation at room temperature. A 0.4 M aqueous solution containing the appropriate amounts of $Ni(NO_3)_2{\cdot}6H_2O$, $Cu(NO_3)_2{\cdot}3H_2O$, $Al(NO_3)_3{\cdot}9H_2O$, and $Mg(NO_3)_2{\cdot}6H_2O$ was added dropwise to a 500 mL three-neck round-bottom flask containing 200 mL of a 0.1 M $Na_2CO_3{\cdot}10H_2O$ under vigorous magnetic stirring. The pH was kept at 9.5 ± 0.1 using a 1.5 M NaOH solution. After complete precipitation, the resulting suspension was aged by conventional refluxing at 80 °C for 20 h. The solids were filtered, washed with deionized water until pH 7, and dried overnight at 80 °C. The nomenclature and the theoretical composition of the synthesized samples are shown in Table 1.

2.3. Preparation of Ni and NiCu supported catalysts

Ni and Ni-Cu catalysts were obtained by calcination of the hydrotalcite precursors at 400 °C in 80 mL/min N_2 flow for 5 h and further reduction at 550 °C under pure H_2 flow at 80 mL/min for 3 h. The resulting catalysts were labeled as CNiAl, CNiMgAl, CNiCuAl and CNiCuMgAl.

The effect of adding Brønsted acidity on the catalytic reaction was evaluated by combining by physical mixing 50 mg of catalysts CNiAl, CNiMgAl, CNiCuAl and CNiCuMgAl with 50 mg of H-βeta, previously prepared. 1 g of commercial Na-βeta zeolite (Zeochem, Si/Al = 10, PB Lot No. 6000186) was treated with NH_4NO_3 1 M at 100 °C for 1 h. After washing several times with deionized water, the sample was calcined at 540 °C for 5 h to obtain the sample called Hβeta. These catalytic systems are named as catalyst name + Hβeta.

To evaluate the effect of Lewis acidity on the catalytic reaction hydrotalcites HT_{NiAl} and HT_{NiCuAl} were impregnated by the wetness impregnation method with an ethanolic solution of NH_4ReO_4 (3 wt% and 5 wt% of Re in the final catalyst). After impregnation, the samples were dried at 80 °C overnight and subsequently calcined at 400 °C for 5 h under N_2 flow (80 mL/min) and finally reduced under H_2 flow at 350 °C for 3 h. Catalysts impregnated with ReOx were labeled as Catalyst Name + Re x%, where x is the weight percentage of rhenium.

2.4. Characterization of the catalytic precursors and catalysts

Elemental analysis of the hydrotalcites was measured using an inductively coupled plasma-original emission spectrometer (ICP-OES) from Spectro Arcos. Before analysis, all samples were digested with concentrated HNO_3. Analyses were made in triplicate.

The structure and crystallinity of the hydrotalcites, fresh and spent catalysts were studied by X-ray diffraction (XRD) measurements using a Bruker-AXS D8-Advance diffractometer equipped with a vertical theta-theta goniometer, 2.5° Soller slits for both incident and diffracted beams, a fixed 0.5° receiving slit, and an automatic air-scattering knife positioned at the sample surface. The angular 2θ range was set from 5° to 80°, with data collected at an angular step of 0.02° and a step time of 0.5 s. Cukα radiation was generated from a copper X-ray tube operating at 40 kV and 40 mA. The diffracted X-rays were detected using a LynxEye-XE-T PSD detector with a 2.94° opening angle. The sample was placed on a low-background silicon (510) support.

All diffractograms were analyzed using the DIFFRAC.EVA 6.0 software from BRUKER.AXS, along with the PDF-2 2022 database from Joint Committee on Powder Diffraction Standards (JCPDS), using the following reference files: 089–0460 for hydrotalcite, 65–2865 for nickel (*syn*-Ni), 70–3039 for copper (*syn*-Cu), 047–1049 for bunsenite (*syn*-NiO), and 77–0199 for cuprite (*syn*-Cu_2O). Relative quantitative phase analysis was performed by Rietveld method. The peak width for each phase was modeled using the Double-Voigt Approach [39], focusing solely on the Lorentzian contribution due to crystallite size and excluding any microstrain effects. The Lorentzian function was used to fit the peaks and obtain the integral breadth. Rietveld refinement was carried out using TOPAS v6 software (Bruker AXS GmbH, 2017), and the background was modeled with a second-order Chebyshev polynomial. The Scherrer equation [40] was then applied to determine the apparent crystallite size.

The surface properties of the catalysts were determined through nitrogen adsorption–desorption isotherms at −196 °C using a 3FLEX MICROMERITICS Adsorption analyzer with a nitrogen molecule cross-sectional area of 0.164 nm^2. B.E.T. theory was applied to calculate the surface area of the materials. Before the analysis, the samples were degassed at 120 °C.

Transmission Electron Microscopy (TEM) was used to study the morphology of the LDHs and catalysts using a JEOL 1011 transmission electron microscope operated at an accelerating voltage of 100 kV with a magnification of 120–400 k. Likewise, morphology was observed by High-Resolution Transmission Electron Microscopy (HRTEM), which was conducted using a JEM-F200 multi-purpose electron microscope equipped with Energy Dispersive X-ray Spectroscopy (EDS). Catalyst powder samples (0.1 mg) were dispersed in ethanol (50 μL) via ultrasonic treatment. The resulting suspension was then deposited onto a carbon-coated copper grid and air-dried before analysis.

Metallic area and metallic dispersion of the catalysts were obtained by H_2 chemisorption, using an AutoChem III (Micromeritics) equipped with a programmable temperature furnace and a calibrated TCD detector. The gas outlet was connected to a quadrupole mass spectrometer. Before the analysis, all the samples were activated at 550 °C for 30 min with pure H_2. The H_2 in excess was removed by flowing He at 15 cm^3/min at 560 °C for 180 min. Then, the sample was cooled down to 30 °C, and the analyses were carried out.

The basic properties of the LDHs were determined by CO_2-TPD using

Table 2
Characterization of the catalytic precursors.

LDHs	Crystallite size (nm) 003 [a]	Crystallite size (nm) 110 [a]	Molar ratio [b]				Chemical formula
			Ni/Al	Cu/Al	Mg/Al	M^{2+}/M^{3+}	
HT_{NiAl}	5.0	9.6	2.97	–	–	2.97	$[Ni_{0.74}Al_{0.25}(OH)_2][(CO_3^{2-})_{0.08}\ (NO_3^-)_{0.07}]\ 0.16\ H_2O$
HT_{NiMgAl}	5.6	10.3	1.98	–	1.00	2.98	$[Ni_{0.50}Mg_{0.25}Al_{0.25}(OH)_2][(CO_3^{2-})_{0.08}\ (NO_3^-)_{0.09}]\cdot 0.16\ H_2O$
HT_{NiCuAl}	3.4	6.3	1.48	1.41	–	2.89	$[Ni_{0.37}Cu_{0.35}Al_{0.25}(OH)_2][(CO_3^{2-})_{0.06}\ (NO_3^-)_{0.07}]\cdot 0.40\ H_2O$
$HT_{NiCuMgAl}$	3.7	5.6	1.00	1.10	1.00	3.10	$[Ni_{0.25}Cu_{0.27}Mg_{0.24}Al_{0.24}(OH)_2][(CO_3^{2-})_{0.08}\ (NO_3^-)_{0.08}]\cdot 0.25\ H_2O$

[a] Calculated from XRD results.
[b] Determined from ICP results.

the AutoChem III equipment (Micromeritics). First, the catalysts were activated at 550 °C for 1 h. Once cooled to 30 °C, the samples were purged with He for 30 min to remove impurities. Afterward, adsorption of CO_2 (3 % volume CO_2 in He at 20 cm^3/min) was conducted for 90 min, followed by a 30-min exposure to a helium flow (20 cm^3/min) at 150 °C to remove weakly adsorbed CO_2. Finally, the temperature was increased to 800 °C at a rate of 5 °C/min while the TCD signal was recorded. A blank for comparison was collected without CO_2 treatment. The basicity of the samples was assessed by analysing the difference between the CO_2 desorption profile obtained after CO_2 adsorption and the decomposition profile of the untreated sample (reference).

X-ray photoelectron spectroscopy (XPS) analysis was conducted to study the surface composition of several catalysts using a ProvenX-NAP system utilizing a monochromatic AlKα (1486.7 eV) x-ray source. The x-ray beam had a spot size of 300 μm of diameter at the sample position. The data were acquired with a PHOIBOS 150 NAP 1D-DLD electron energy analyzer (SPECS GmbH, Berlin) under ultra-high vacuum ($\sim 1\cdot 10^{-9}$ mbar), using a 60 W x-ray power, 30 eV pass energy, and 7x20 mm entrance slit with an open mesh exit slit. Before analysis, the catalysts were activated in H_2 flow at 550 °C for 1 h and mounted on a stainless-steel holder with double-sided carbon tape. Additionally, data processing was performed using CasaXPS software, focusing on the Ni2p, Cu2p, C1s, and O1s binding energies. The binding energies were adjusted relative to the C1s peak at 284.8 eV, and a Shirley background was applied, with core-level lines fitted using a Gaussian-Lorentzian GL (30) model. Each sample was measured at a 0° emission angle relative to the surface normal. Based on typical values for the electron attenuation length of relevant photoelectrons, the XPS analysis depth ranges between 5 and 10 nm on a flat surface.

Fourier Transform Infrared (FTIR) spectroscopy measurements were performed on fresh and spent catalysts using a Jasco FT/IR-6700 spectrometer equipped with a diamond crystal in Attenuated Total Reflectance (ATR) mode. The spectral range was set from 4000 to 400 cm^{-1}, with a resolution of 4 cm^{-1}. Each spectrum represents the average of 32 scans to ensure an optimal signal-to-noise ratio.

2.5. Catalytic activity

Catalyst tests were carried out in a 100 mL batch reactor with stirring at 700 rpm to avoid external diffusion limitations. In a typical experiment, the reactor contained 200 mg of guaiacol, 40 mL of n-dodecane, and 100 mg of catalyst (Guaiacol/catalyst wt. ratio = 2). The reaction was carried out at 300 °C under 50 bar of H_2 for 1 h with a heating ramp of 5 °C/min. Afterwards, the reaction was quenched with an ice bath, and the products were filtered and analyzed by gas chromatography using a Shimadzu GC-2010 instrument equipped with a TRB-PETROL column (100 m × 0.25 mm × 0.50 μm) with a flame ionization detector (FID). Quantification was conducted with calibration lines using hexadecane as the internal standard. The guaiacol conversion and the selectivity towards the reaction products were calculated using the following equations:

$$\%\,\text{Conversion} = \frac{\text{number of moles of converted guaiacol}}{\text{number of moles of initial guaiacol}} \times 100$$

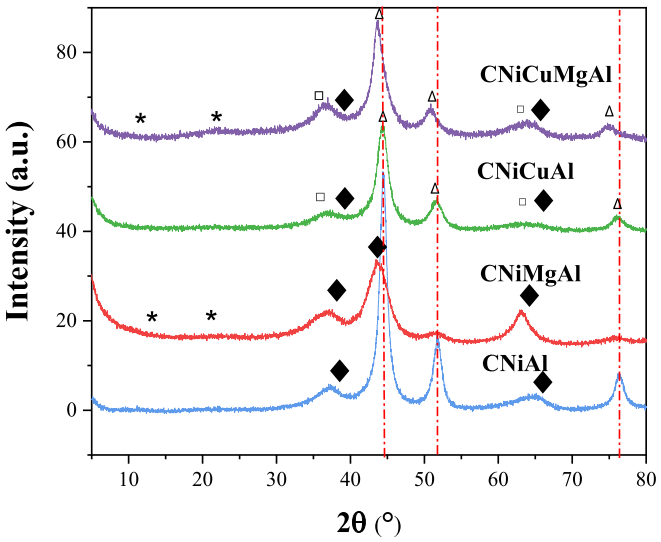

Fig. 1. XRD patterns of the catalysts. Crystalline phases: (◆) NiO, (-·-) Ni, (□) Cu_2O, (Δ) NiCu alloy, (*) Hydrotalcite phase.

$$\%\text{Selectivity} = \frac{\text{number of moles of guaiacol converted to the reaction product}}{\text{number of moles of converted guaiacol}} \times 100$$

3. Results and discussion

3.1. Effect of the acid-base properties of the Ni and NiCu catalysts, obtained from LDHs, on the hydrodeoxygenation of guaiacol

XRD patterns of the catalytic precursors showed only the presence of the crystalline hydrotalcite phase (Fig. S1a), as confirmed by TEM and HRTEM microscopy (e.g. Fig. S1b,c) where the characteristic layered and platelet hydrotalcite structure was observed. Cu-containing hydrotalcites (HT_{NiCuAl} and $HT_{NiCuMgAl}$) had lower crystallite size both in the stacking and in the lamella direction than HT_{NiAl} and HT_{NiMgAl} (Table 2). This can be explained by the Jahn-Teller effect of Cu^{2+}, which makes more difficult its incorporation into the brucite-like layers [41,42].

The composition of the LDHs, determined by elemental analysis (Table 2), mostly agreed with the theoretical cations molar ratio values (Table 1). Their chemical formula was calculated from the experimental cations molar ratio values, the carbonate content was determined from decomposition studies with a calibrated detector, and the number of nitrates as the anions necessary to compensate the positive charge of the layers (Table 2).

XRD patterns of catalysts revealed the disappearance of the hydrotalcite structure after the calcination and reduction processes (Fig. 1). For the catalysts containing magnesium, CNiMgAl and CNiCuMgAl, very small amounts of amorphous hydrotalcite phase were also detected (Fig. 1).

Table 3
Characterization of the catalysts obtained from hydrotalcite-like materials.

Catalysts	Crystalline metallic phases (%)[a]				Crystallite size (nm)[a]				BET surface area [b] (m^2/g)	Metallic area [c] (m^2/g)	Dispersion (%) [c]
	Ni	NiCu alloy	NiO	Cu_2O	Ni	NiCu alloy	NiO	Cu_2O			
CNiAl	63	–	37	–	6.1	–	1.6	–	121	43	46
CNiMgAl	17	–	83	–	3.5	–	1.8	–	112	26	21
CNiCuAl	–	47	39	14	–	3.8	1.5	1.4	103	4	4
CNiCuMgAl	–	22	53	25	–	3.5	1.9	1.5	118	2	1

[a] Calculated from XRD results.
[b] Determined by N_2 physisorption.
[c] Calculated from H_2 chemisorption.

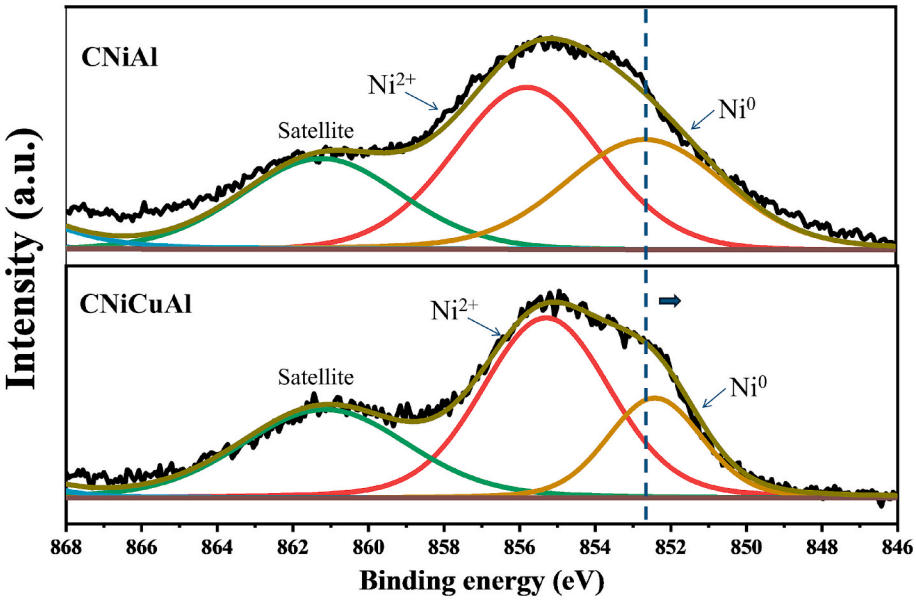

Fig. 2. Ni $2p_{3/2}$ XPS spectra for CNiAl and CNiCuAl catalysts.

Monometallic catalysts, CNiAl and CNiMgAl, had a metallic Ni crystalline phase together with some unreduced NiO phase, in higher amounts for CNiMgAl (Fig. 1). For the bimetallic catalysts, the incorporation of Cu atoms into the Ni lattice provoked the enlargement of the lattice, as confirmed by the shift to lower 2θ values observed for CNiCuAl (44.18°) and CNiCuMgAl (43.62°) in comparison with that corresponding to the metallic Ni phase at 44.5° (see red discontinuous line in Fig. 1). This could indicate the formation of a NiCu alloy. The NiCu ratio calculated from the cell parameter of the NiCu alloy phase according to the Vegard's law for these catalysts was $Ni_{5.6}Cu$ for CNiCuAl and $NiCu_{2.4}$ for CNiCuMgAl. Cu_2O phase was also detected in addition to unreduced NiO for these bimetallic catalysts. Metallic Cu was not observed in any case.

The percentage of each crystalline phase was calculated using TOPAS V6 software by Rietveld refinement while the crystallite size was determined using the Scherrer equation (Table 3). The metallic content was higher for the samples without Mg (CNiAl and CNiCuAl). Regarding crystallite sizes, the Ni crystallite size in the CNiAl catalyst was larger (6.1 nm) than that of the CNiMgAl catalyst (3.5 nm) and those of the NiCu alloy obtained for the bimetallic catalysts (3.5–3.8 nm) (Table 3). The variations observed in the amount and crystallinity of the metallic phases, and in the composition of the NiCu alloy can be attributed to differences in the reducibility of their catalytic precursors, which in turn are influenced by their composition. Thus, the catalysts derived from a precursor containing magnesium presented higher amounts of NiO and Cu_2O oxide species compared to those without it. This could be attributed to a higher interaction of Ni and Cu cations with the Mg-Al mixed oxides, which hinders their reduction, especially for Ni. This also explains the higher content of Ni in the $Ni_{5.6}Cu$ alloy for CNiCuAl.

XPS of the CNiAl and CNiCuAl catalysts allowed us to confirm the formation of the NiCu alloy. The Ni $2p_{3/2}$ spectra for both catalysts are shown in Fig. 2. Two peaks at 852.7 eV and 855.8 eV, assigned to Ni^0 and Ni^{2+} species, respectively were observed in the Ni $2p_{3/2}$ spectrum of CNiAl catalyst (Fig. 2). This assignment agrees with XPS results obtained for hydrotalcite-type materials [43,44]. The shift to lower BE values of the metallic Ni peak observed for the CNiCuAl catalyst (852.4 eV) indicates electron transfer from Cu to Ni. This could be attributed to the formation of the NiCu alloy, as previously reported [43,45]. These XPS results also confirmed the presence of higher amounts of Ni for CNiAl than for CNiCuAl, as previously observed by XRD.

N_2 adsorption-desorption isotherms of the catalysts were of type IV corresponding to mesoporous materials according to IUPAC classification leading to surface areas in the range 103–121 m^2/g (Table 3).

The metallic area and dispersion of the catalysts, determined by H_2 chemisorption, are also shown in Table 3. Among the samples, CNiAl displayed the highest metallic area (43 m^2/g) followed by CNiMgAl (26 m^2/g) while the bimetallic NiCu catalysts showed low metallic areas (2–4 m^2/g). The differences between monometallic and bimetallic catalysts could be attributed to the poor H_2 adsorption of Cu compared to Ni [46]. The lower metallic area of CNiMgAl relative to CNiAl could be attributed to its lower Ni content (Table 3). The Ni-rich alloy in catalyst CNiCuAl ($Ni_{5.6}Cu$) led to higher metallic area when compared to CNiCuMgAl with an alloy richer in Cu ($NiCu_{2.4}$).

Transmission electron microscopy (TEM) was employed to examine the morphology of the catalysts. As example, the micrographs of the CNiAl and CNiCuAl catalysts with their particle size distributions are

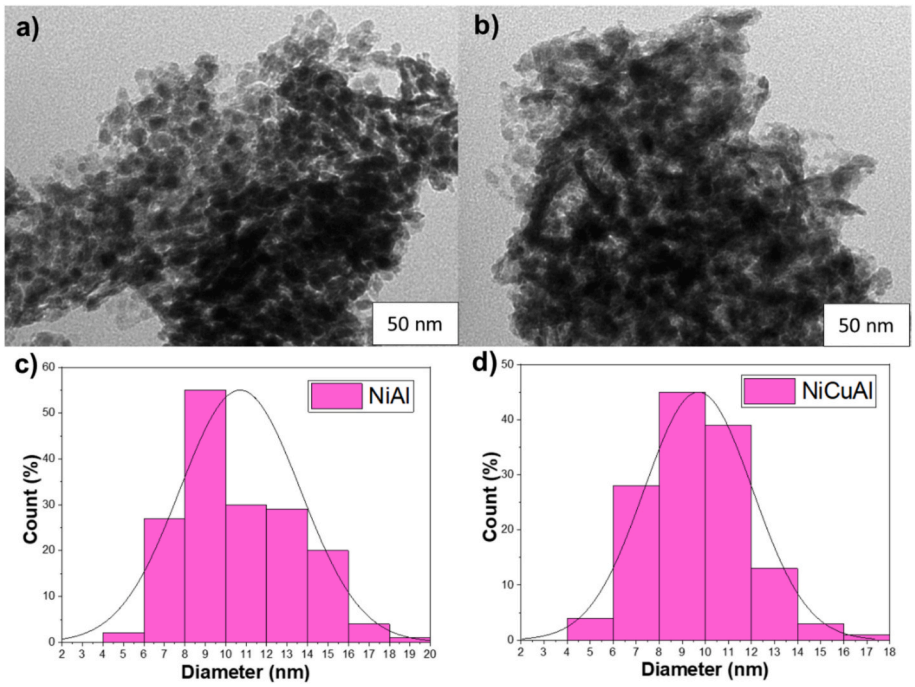

Fig. 3. TEM images of CNiAl (a), CNiCuAl (b) with their respective particle size distributions (c,d).

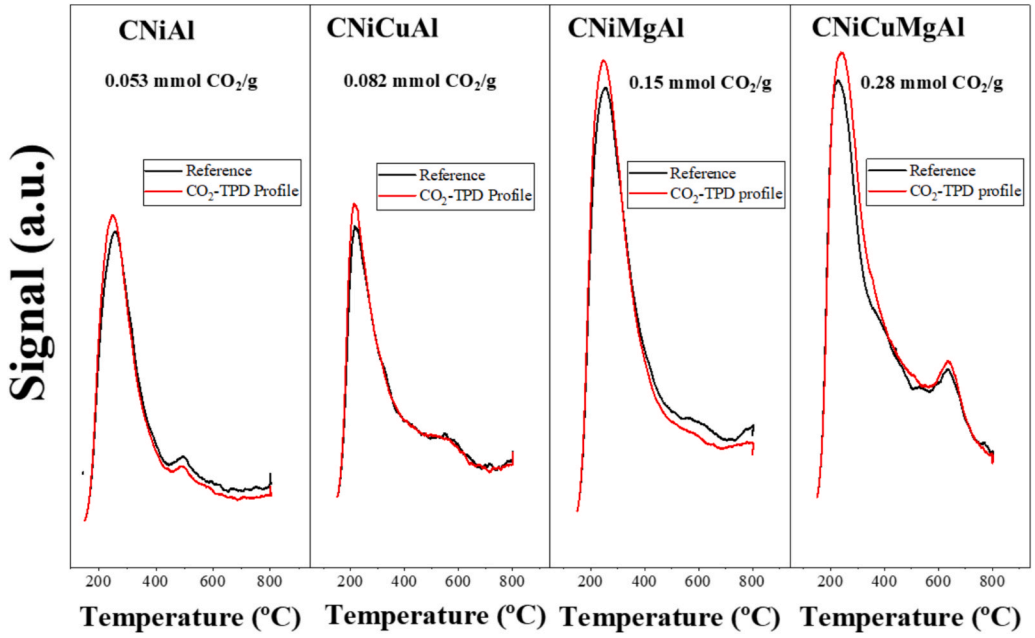

Fig. 4. CO_2-TPD profiles of the catalysts.

shown in Fig. 3. The hydrotalcite layered structure disappeared after calcination of the LDHs and subsequent reduction, as expected, and highly dispersed metallic nanoparticles supported on a mixed oxide were observed. The size distribution of the particles exhibited a unimodal Gaussian distribution profile for both catalysts with an average diameter slightly higher for CNiAl (10.7 nm) than for CNiCuAl (9.7 nm). Additionally, a more homogeneous Gaussian profile was observed for the bimetallic catalytic system. This can be explained by the presence of the NiCu alloy.

The basicity properties of the catalysts were investigated through CO_2-TPD analysis (Fig. 4). The monometallic catalyst CNiAl, exhibited a profile with a broad peak between 200 °C and 500 °C. The quantification of the basic sites for this catalyst showed a low number (0.05 mmol CO_2/g). For CNiCuAl, a similar profile was observed with a slightly higher number of basic sites (0.082 mmol CO_2/g) than its monometallic counterpart. Upon introduction of Mg in CNiMgAl and CNiCuMgAl catalysts, a significant increase in the number of basic sites was obtained (0.15 mmol CO_2/g and 0.28 mmol CO_2/g, respectively). This should be related to the presence of magnesium mixed-oxide species, which led to higher basicity.

Regarding catalytic activity, first, the optimization of several reaction parameters focusing on the selective obtention of cyclohexane was conducted for catalyst CNiAl (Fig. S2) considering the parameter values mainly used in the literature for this reaction at temperatures > 200 °C

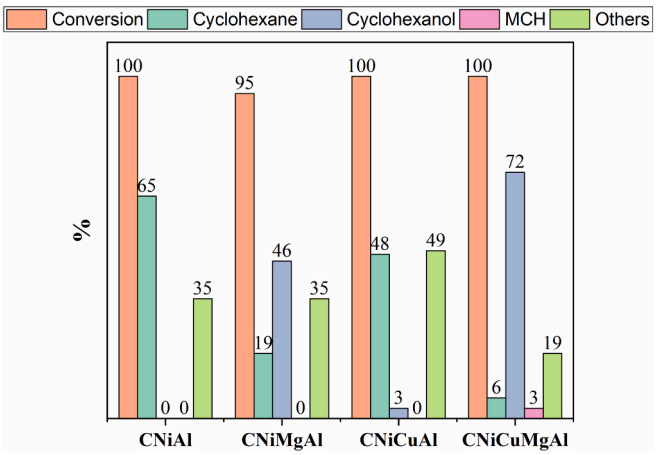

Fig. 5. HDO of guaiacol of the catalysts with 50 bar of H_2 at 300 °C for 1 h. Guaiacol/catalyst weight ratio = 2.

[4,10] and maintaining the pressure of H_2 at 50 bar. At 300 °C, the catalyst led to high selectivity to cyclohexane (65 %) for a complete conversion (Fig. S2a). When the temperature was decreased to 240 °C, the formation of cyclohexane was significantly reduced to 3 %, obtaining cyclohexanol (31 %) and methoxycyclohexanol (30 %) as main reaction products (Fig. S2a). This indicates that deoxygenation and demethoxylation processes were not favored at lower temperature and that more energy is required to overcome these steps. By comparing at 300 °C for 1 h or 2 h of reaction (Fig. S2b) comparable catalytic results were obtained. Finally, by varying the guaiacol/catalyst weight (wt) ratio, for 1.5 and 2 the results were similar (Fig. S2c) while at guaiacol/catalyst wt ratio > 2, the formation of cyclohexane decreased, as expected, at the benefit of the formation of cyclohexanol and other reaction products since dehydration and hydrogenation reactions were not favored due to the relative lower number of active sites. The high conversion values observed in all tests denote the high reactivity of guaiacol in these reaction conditions.

The catalytic activity of the four catalysts, derived from the LDHs previously prepared, for the hydrodeoxygenation of guaiacol using the optimized conditions at 300 °C, 50 bar of H_2 for 1 h with guaiacol/catalyst weight ratio of 2 is shown in Fig. 5.

High guaiacol conversion was obtained for all catalysts being the main products cyclohexane or cyclohexanol depending on the catalyst composition. Notably, cyclohexane was the main product (48–65 %) for those catalysts that did not contain Mg (CNiAl and CNiCuAl). This result is significant since the obtention of cyclohexane has not been reported before for this reaction using catalysts obtained from hydrotalcite-type materials. Besides, these selectivity values to cyclohexane were higher than those previously reported for other catalysts tested at the same reaction conditions (300 °C, 50 bar, 1 h). Thus, Ni-Mg(5 %)/AC catalyst led to 20 % of cyclohexane for a 30 % of conversion [16] while using Cu-ZnO-Al_2O_3 catalyst, 20 % of cyclohexane yield was obtained for a 76 % of conversion, in this case, at 2 h of reaction [17].

Monometallic CNiAl catalyst presented higher selectivity towards cyclohexane (65 %) compared to its bimetallic counterpart CNiCuAl (48 %). This can be related to the higher metallic content and higher metallic area of catalyst CNiAl (Table 3). Interestingly, when the catalysts with Mg were tested, the selectivity changed and cyclohexanol was the main product. CNiMgAl had 46 % of selectivity to cyclohexanol while its bimetallic counterpart, CNiCuMgAl, led to 72 %. This could be related to the higher basicity of these catalysts (Fig. 4), due to the presence of MgOx species, which has been reported to inhibit dehydration processes for this reaction [30]. The more basic the catalytic system, the greater the selectivity towards cyclohexanol. The best selectivity to cyclohexanol (72 %) was higher than those reported previously for other catalysts tested at the same reaction conditions (300 °C, 50 bar, 1 h) since 50 % of cyclohexanol selectivity and 35 % of cyclohexanol yield were obtained with Ni-Mg(5 %)/AC and Cu-ZnO-Al_2O_3 catalysts, respectively [16,17], this later at 2 h of reaction. The fact that methoxycyclohexanol (MCH) was detected in small amounts for one of the catalysts, could suggest that the reaction followed the direct hydrogenation route and further demethoxylation and hydrogenolysis processes (Scheme 2).

In the literature, the most of Ni-based catalysts tested for the HDO of guaiacol favored the formation of MCH at low temperatures (< 200 °C) while at higher temperatures (> 200 °C) inhibited such reaction at the benefit of phenol formation [47,48]. In the present work, the presence of methoxycyclohexanol cannot be attributed to the reaction conditions but to the properties of the Ni and NiCu catalysts obtained from layered double hydroxides. This pathway was previously identified by Dongil et al. [48] when using Ni/C nanotubes catalysts at 300 °C, 50 bar of H_2 for 4 h. These authors proposed that some catalytic systems could promote the transport of H_2 by spillover favoring the formation of MCH at these harder conditions [48]. Later demethoxylation of MCH to cyclohexanol can be done on the basic centres of these catalysts, as previously reported [30]. The use of high temperature and pressure has been shown to weaken/break the C-O bond favoring the formation of cyclohexene, which can be then fast hydrogenated by the metallic centers to cyclohexane [29]. It is important to note that acidity does not play a role on the catalytic results obtained with these catalysts since they did not show practically acidity. For instance, catalyst CNiAl, without magnesium, showed a negligible acidity, 0.0015 mmol NH_3/g, as calculated from NH_3 TPD.

The obtention of cyclohexane and cyclohexanol varying the composition highlights that hydrotalcite-like materials are excellent catalytic precursors. Furthermore, the ability of non-Mg catalysts derived from hydrotalcites to selectively yield cyclohexane has not been reported before and remarks their potential in applications where fully deoxygenated, fuel-ready products are required. Thus, optimizing catalyst compositions to promote cyclohexane production offers a promising pathway for advancing biomass conversion technologies.

In order to evaluate and compare the selectivity of the catalysts at lower conversion values, their catalytic activity was checked using lower amount of catalyst (25 mg) for a shorter reaction time (0.5 h), maintaining the rest of the reaction conditions (Fig. S3). By decreasing conversion, a decrease in the selectivity to cyclohexane, accompanied by an increase in the formation of the oxygenated intermediates, cyclohexanol and methoxycyclohexanol, was observed for all catalysts. This shows the importance of the reaction conditions in controlling the degree of hydrodeoxygenation. It is important to remark that, despite the lower

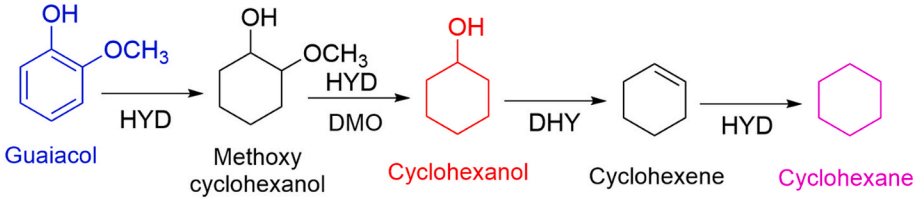

Scheme 2. Reaction pathway proposed for the catalysts obtained from LDHs. DMO: Demethoxylation, HYD: Hydrogenation, DHY: Dehydration.

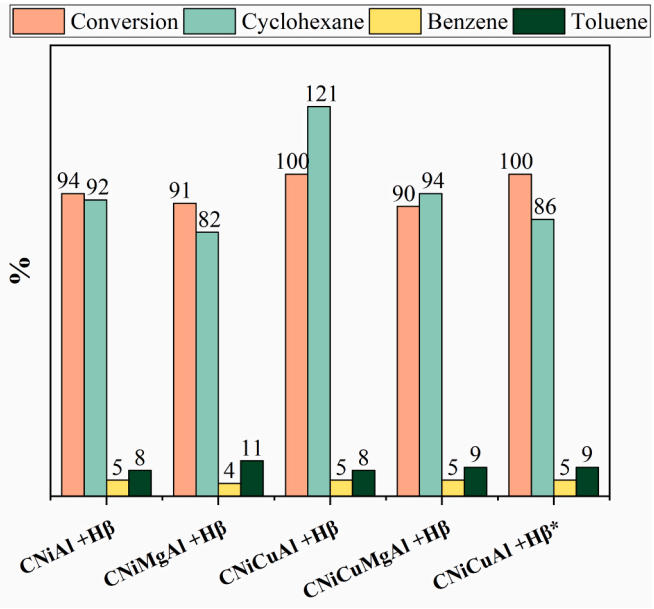

Fig. 6. HDO of guaiacol of catalysts combined with Hβ zeolite under 50 bar of H_2 at 300 °C for 1 h. Guaiacol/catalyst weight ratio = 2. * Reaction carried out without guaiacol.

conversion values, it was possible to obtain cyclohexane in three of the four catalysts. This has not been previously observed for catalysts obtained from hydrotalcite-like materials at any reaction conditions. Additionally, CNiAl and CNiCuAl showed higher selectivity to cyclohexane than their corresponding containing Mg catalysts, keeping the same tendency observed in Fig. 5, where the presence of Mg influenced the reaction pathway, promoting the partial deoxygenation to cyclohexanol. These catalytic results also confirmed the proposed pathway for these catalysts, as evidenced by the higher amounts of methoxycyclohexanol obtained under these lower conversion conditions.

3.2. Effect of adding BrØnsted acid sites to the catalytic systems obtained from LDHs

When hydrodeoxygenation of guaiacol was studied at low reaction temperature (< 200 °C), BrØnsted acidity played an important role, promoting demethoxylation and dehydration processes for obtaining cyclohexane [49,50]. Thus, Wang et al. [49] obtained 91.7 % of yield to cyclohexane using a Ni/SiO_2 catalyst combined with Hβ zeolite at 140 °C, 30 bar of H_2 for 2.5 h. Casadó et al. [50] achieved 78 % of cyclohexane selectivity for a complete conversion with a Ni/ordered mesoporous carbon combined with Hβ at 180 °C, 30 bar of H_2 for 1 h.

To study the influence of BrØnsted acidity at higher temperature and pressure, the four catalysts obtained from LDHs were combined with Hβ zeolite and tested with the same reaction conditions than the catalysts alone: 50 bar of H_2, guaiacol/catalyst wt ratio of 2, at 300 °C for 1 h. The results are shown in Fig. 6.

Very high selectivity to cyclohexane for a very high conversion was achieved with all the catalytic systems. Surprisingly, the selectivity to cyclohexane calculated using the calibration lines for catalyst CNiCuAl + Hβ was higher than 100 %. This result suggests that other compounds present in the reaction were likely transformed to cyclohexane. To check this option, the reaction was carried out without guaiacol at the same reaction conditions with catalyst CNiCuAl + Hβ obtaining 86 % of selectivity to cyclohexane for a total conversion (Fig. 6). These results suggested that the BrØnsted acidity provided by Hβ converted the solvent dodecane to cyclohexane at these reaction conditions. When other solvents, such as decane, were tested, the same behavior was observed. Therefore, we can conclude that all these catalysts combined with Hβ overproduced cyclohexane due to the additional reaction of the solvent used at the reaction conditions tested. Interestingly, some amounts of benzene and toluene were also detected for all catalysts. Methoxycyclohexanol was not observed in any case. This indicates that the catalysts combined with Hβ followed a different reaction pathway (Scheme 3) compared to the pathway followed by the catalysts alone (Scheme 2).

Thus, BrØnsted acid sites were responsible for demethoxylation, transalkylation, and dehydration reactions while metallic ones catalyzed the hydrogenation reactions. This agrees with the mechanism proposed by Lee et al. for Pt/HY, Pt/H-Beta and Pt/H-ZSM-5 catalysts, which had metallic and BrØnsted acid centers for the hydrodeoxygenation of guaiacol to cyclohexane at 250 °C, 40 bars of H_2 for 2 h [14,25]. The authors did not report overproduction of cyclohexane probably due to the lower temperature used.

3.3. Effect of adding Lewis acid sites to the catalytic systems obtained from LDHs

The effect of the Lewis acidity on the HDO of guaiacol to cyclohexane has not been practically explored. Considering that catalysts CNiAl and CNiCuAl led to the highest selectivity to cyclohexane (Fig. 5), their corresponding hydrotalcites were modified with ReOx to have in the final catalysts 3 wt% and 5 wt% of Re. Low rhenium contents were chosen to minimize the redox activity of the ReOx species [13].

XRD patterns of the catalysts with different rhenium loading are

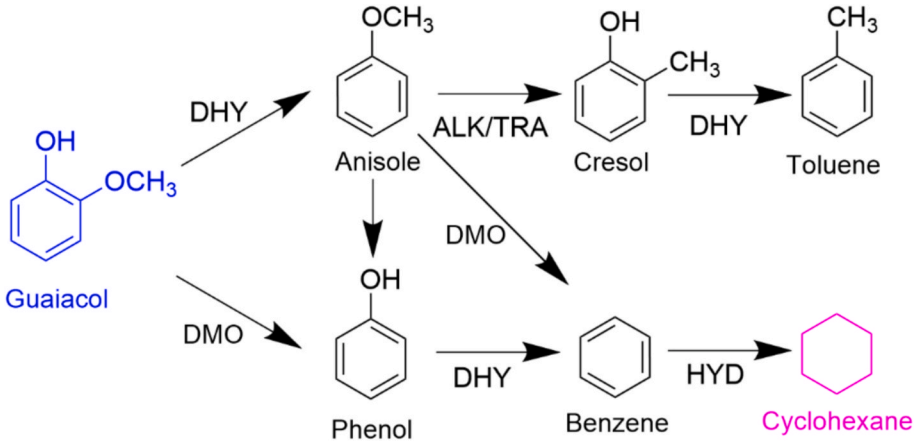

Scheme 3. Hydrodeoxygenation pathway proposed for the catalysts obtained from LDHs combined with H-βeta. DMO: Demethoxylation, HYD: Hydrogenation, DHY: Dehydration, ALK/TRA: Transalkylation.

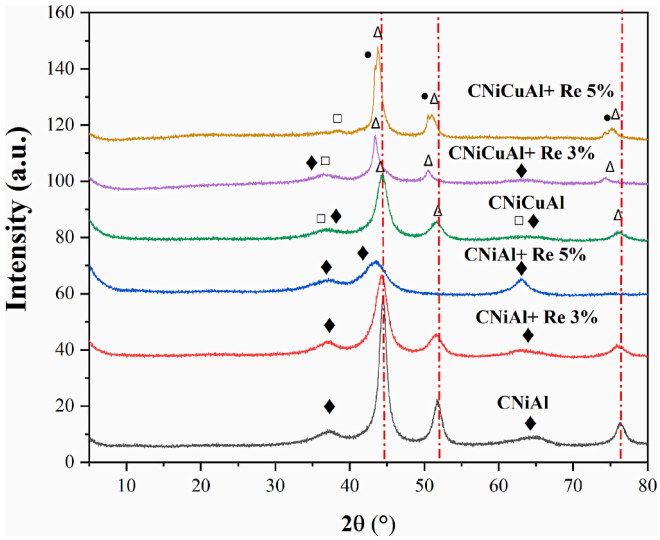

Fig. 7. XRD patterns of the reduced catalysts with ReOx. Crystalline phases: (◆) NiO, (-·-) Ni, (□) Cu_2O, (Δ) NiCu alloy, Cu (●).

shown in Fig. 7 compared to the corresponding catalysts without rhenium. The quantification of the crystalline phases and their crystallite size, obtained from XRD, are indicated in Table 4.

The increase of rhenium content in CNiAl decreased the amount of metallic Ni, with respect to NiO, and reduced its crystallinity (Table 4). However, for CNiCuAl, higher rhenium content led to the formation of higher amounts of more crystalline NiCu alloy (Table 4) in addition to the Cu_2O and NiO phases for CNiCuAl + Re 3 %, and to the Cu_2O and Cu phases for CNiCuAl + Re 5 %. This indicates that the addition of rhenium decreased the reducibility to Ni for monometallic catalysts and increased the reducibility to NiCu alloy and Cu for the bimetallic ones. Interestingly, the Cu content in the NiCu alloy increased as the rhenium amount increased. Thus, for catalyst, CNiCuAl + Re 5 %, the composition of the alloy was $NiCu_{1.15}$. This confirms the effect of rhenium in the reducibility to Ni since the composition for the catalyst CNiCuAl, without rhenium, was richer in Ni ($Ni_{5.6}Cu$).

XPS experiments were carried out to study the effect of rhenium in the reducibility of the oxide phases at surface level. Thus, the peaks of the Ni $2p_{3/2}$ XPS spectrum corresponding to metallic Ni (853.1 eV) and Ni^{2+} (856.4 eV) for catalyst CNiAl, shifted towards lower binding energy values, (852.4 eV for Ni and 855.4 eV for Ni^{2+}) for the catalysts with Re, e.g. CNiAl + Re 5 % (Fig. 8). This could be attributed to the possible electron transference from Re to Ni. Furthermore, a decrease in the amount of Ni, accompanied by an increase of NiO was observed for the catalysts with Re in agreement with the results obtained by XRD. For the bimetallic catalyst, CNiCuAl, the peaks of the Ni $2p_{3/2}$ XPS spectrum corresponding to metallic Ni and Ni^{2+} (Fig. 8) and the peaks of the Cu $2p_{3/2}$ spectrum (Fig. 9) practically did not shift after rhenium addition. However, a decrease in the amount of metallic Ni was also observed (Fig. 8). Moreover, the Ni $2p_{3/2}$ XPS spectrum of catalyst CNiCuAl + Re 5 % showed the presence of surface Ni^{2+} species, probably NiO, which was not detected by XRD (Fig. 7).

Due to the close binding energies of Cu $2p_{3/2}$ for the Cu^+ and Cu^0, the Auger electron spectroscopy (AES) of Cu LMM was carried out to distinguish between them (Fig. 9, right). Thus, the peaks at 568.3 and 571.3 eV corresponded to Cu^0 and Cu^+ species, respectively, being Cu^0 the main one. This agrees with the differences observed by XRD when calculating the NiCu content of the catalysts since the NiCu alloy was richer in Cu for CNiCuAl + Re 5 % while the NiCu alloy was richer in Ni for CNiCuAl catalyst.

Table 4
Characterization of the catalysts obtained from hydrotalcite-like materials with Re compared to their counterpart without Re.

Catalysts	Crystalline metallic phases (%)[a]					Crystallite size (nm)[a]				
	Ni	NiCu alloy	NiO	Cu_2O	Cu	Ni	NiCu alloy	NiO	Cu_2O	Cu
CNiAl	63	–	37	–	–	6.1	–	1.6	–	–
CNiAl + Re 3 %	57	–	43	–	–	3.7	–	1.6	–	–
CNiAl + Re 5 %	6	–	94	–	–	3.2	–	1.6	–	–
CNiCuAl	–	47	39	14	–	–	3.8	1.5	1.4	–
CNiCuAl + Re 3 %	–	58	33	9	–	–	4.8	1.4	2.1	–
CNiCuAl + Re 5 %	–	80	–	8	12	–	6.4	–	3.2	36

[a] Calculated from XRD results.

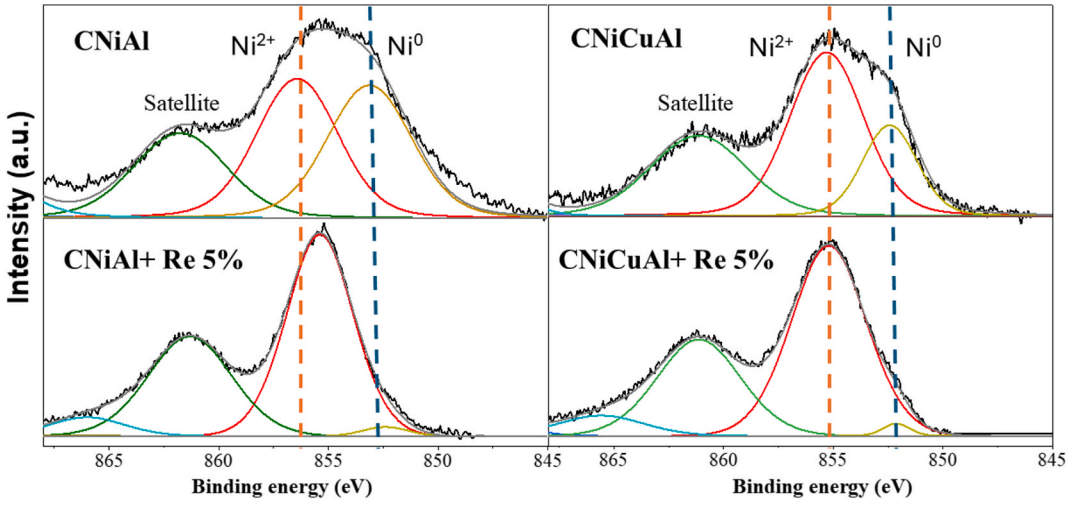

Fig. 8. Ni $2p_{3/2}$ XPS spectra of 5 % Re modified CNiAl and CNiCuAl catalysts. The blue dotted in lines indicates the position of metallic Ni and orange dotted lines indicates the position of the oxidized species.

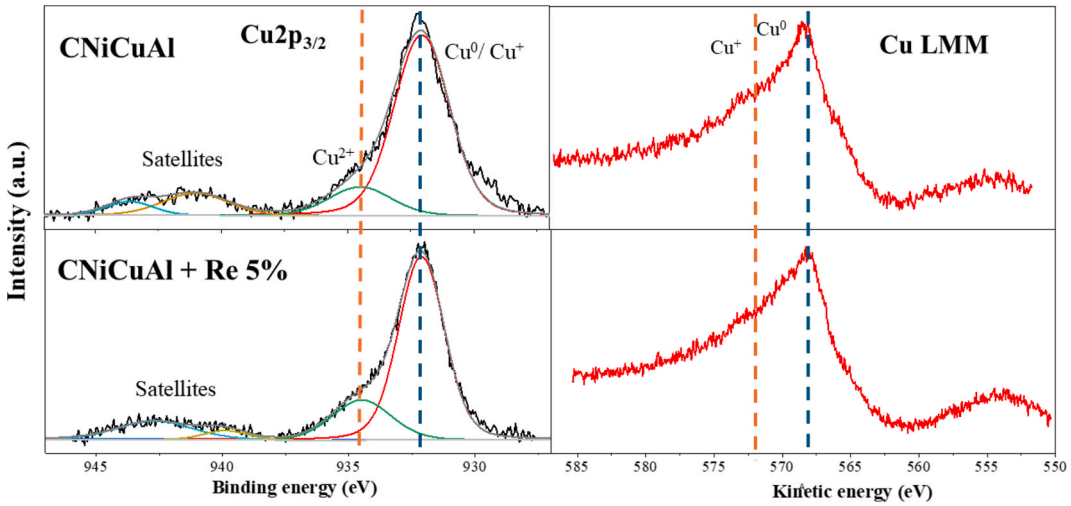

Fig. 9. Cu $2p_{3/2}$ XPS spectra of fresh and ReOx modified CNiCuAl catalyst (left) and their corresponding Auger lines (right). The blue dotted line indicates the position of metallic Cu and the orange dotted line indicates the oxidized species.

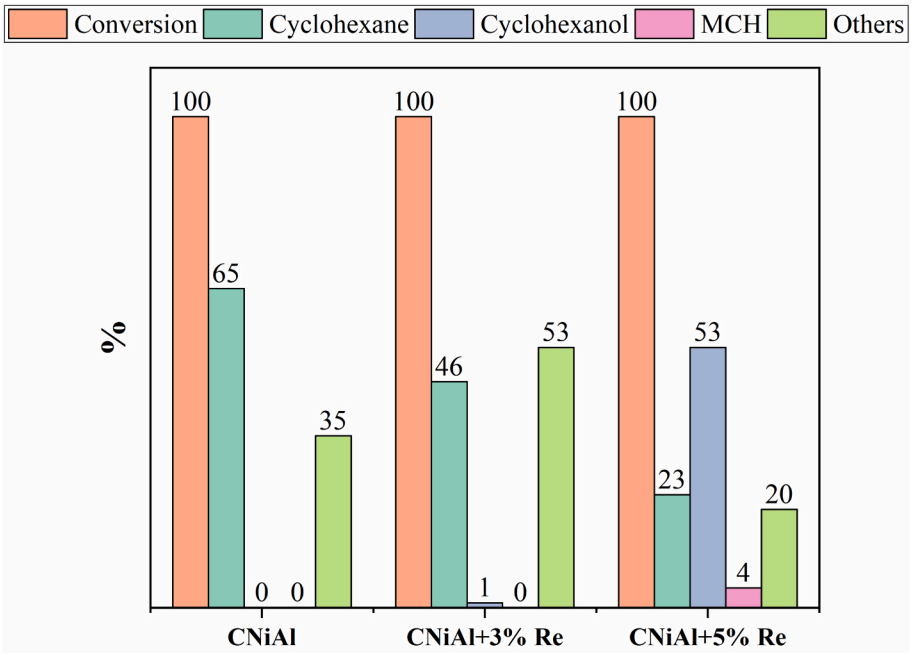

Fig. 10. HDO of guaiacol with CNiAl catalysts with and without ReOx. Reaction conditions: 300 °C under 50 bar of H_2 for 1 h. Guaiacol/catalyst wt ratio of 2.

Fig. 10 shows the catalytic activity of the CNiAl catalysts with different Re loading and without Re for comparison on the hydrodeoxygenation of guaiacol at 300 °C for 1 h, 50 bar of H_2 and guaiacol/catalyst weight ratio of 2.

The modification of the CNiAl with rhenium did not affect conversion, which remained complete. However, the reaction product distribution changed significatively. The selectivity to cyclohexane decreased progressively in the order CNiAl > CNiAl + Re 3 % > CNiAl + Re 5 %. This can be explained by the decrease in the amount of metallic Ni, as observed by XRD (Fig. 7, Table 4) and XPS (Fig. 8). At higher Re loading, cyclohexanol was the main product (53 %) and methoxycyclohexanol was detected in low amounts. The presence of higher amounts of Lewis acid sites (ReOx) for this catalyst could facilitate the binding of the oxygenated compounds, as proposed by P. He et al [6].

For the bimetallic catalytic system, CNiCuAl with and without rhenium, the same behavior concerning the obtention of cyclohexane was observed (Fig. 11).

Although in this case the amount of metallic phase increased with the rhenium content (Table 4), the fact that the NiCu alloy was richer in Cu, a metal with less hydrogenation ability, for the catalysts modified with Re limited their effectiveness for obtaining cyclohexane. However, the highest selectivity to cyclohexanol was achieved for the catalyst CNiCuAl + 3 % Re. The presence of reduced Cu, with high crystallite size in catalyst CNiCuAl + 5 % Re (Table 4) could favor the formation of other reaction products. The lower selectivity to cyclohexanol of these catalytic bimetallic systems with Re with respect to the bimetallic catalyst CNiCuMgAl (Fig. 5) confirmed that as richer in Cu the NiCu alloy was, the higher the selectivity to cyclohexanol was observed.

The presence of methoxycyclohexanol in one of the catalysts modified with rhenium (Fig. 10) together with the absence of other possible reaction products such as benzene or toluene, allowed us to think that these catalytic systems with additional Lewis acid sites followed the reaction pathway proposed in Scheme 2.

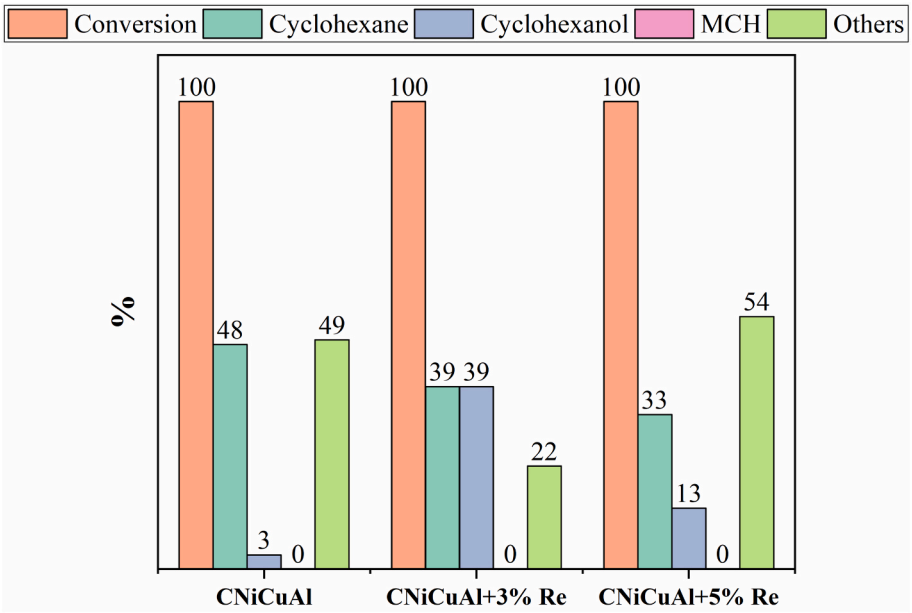

Fig. 11. HDO of guaiacol with CNiCuAl catalysts with and without ReOx. Reaction conditions: 300 °C under 50 bar of H_2 for 1 h. Guaiacol/catalyst wt ratio of 2.

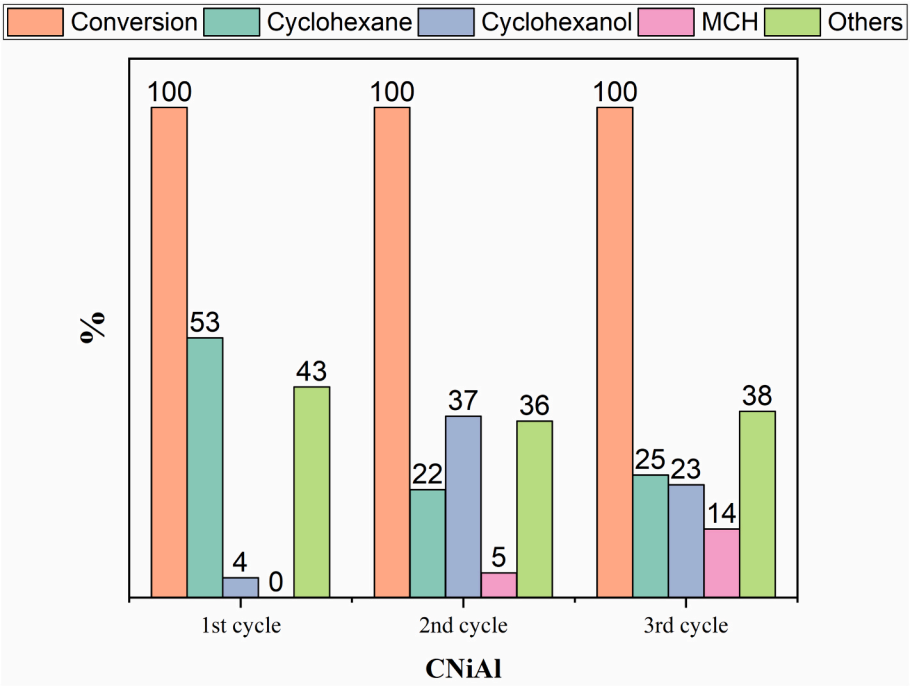

Fig. 12. Reutilization studies of catalyst CNiAl. Reaction conditions: 300 °C, 50 bar of H_2 for 1 h. Guaiacol/catalyst wt ratio of 2.

3.4. Reusability tests and characterization of spent catalysts

In order to check the stability of the catalysts obtained from layered double hydroxides, the reusability of the catalysts CNiAl and CNiCuAl, which were the most selective to cyclohexane, was studied by performing 3 cycles using the reaction conditions of 300 °C, 50 bar of H_2 for 1 h with guaiacol/catalyst wt ratio of 2 (Figs. 12 and 13). After each reaction, the catalyst was filtered, washed with the solvent dodecane and dried at 80 °C before using for the next run.

Conversion remained constant after 3 cycles for both catalysts. However, some variations in the selectivity values were observed. Thus, after the second cycle, the selectivity to cyclohexane decreased, especially for catalyst CNiAl, at benefit of the formation of cyclohexanol. Additionally, methoxycyclohexanol was detected in low amounts for both catalysts. This confirms that the pathway these catalytic systems follow is proposed in Scheme 2. For the 3rd cycle, the differences with respect to the 2n cycle were lower for both catalysts. To explain these results, spent catalysts were characterized after reaction and compared with fresh catalysts by XRD (Fig. 14).

XRD pattern of the spent CNiAl catalyst (Fig. 14a) showed the presence of Ni and NiO phases, as in the fresh catalyst, but with lower amount of less crystalline Ni (34 %). This could explain the decrease in the selectivity to cyclohexane observed after 2nd reuse (Fig. 12). On the other hand, XRD pattern of spent CNiCuAl catalyst (Fig. 14b) exhibited

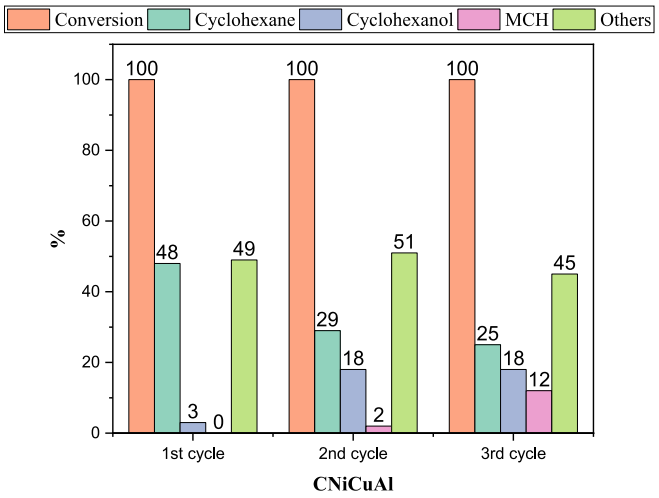

Fig. 13. Reutilization studies of CNiCuAl catalyst. Reaction conditions: 300 °C, 50 bar of H_2 for 1 h. Guaiacol/catalyst wt ratio of 2.

higher amounts of higher crystalline NiCu alloy (64 %) than fresh CNiCuAl catalyst (47 %), in addition to NiO and Cu_2O phases also present in the fresh catalyst. The composition of the NiCu alloy for the spent CNiCuAl catalyst was $NiCu_{1.5}$. This could justify the decrease in the selectivity to cyclohexane observed since fresh CNiCuAl had an alloy richer in Ni ($Ni_{5.6}Cu$), and therefore with higher hydrogenation ability.

In order to analyze the possible adsorption of reaction products which limited the catalytic activity of the active sites during reuse, the FTIR spectra of the fresh and spent CNiAl catalysts were performed (Fig. 15).

The spectrum from the fresh CNiAl catalyst revealed a peak at 3326 cm^{-1} corresponding to O–H stretching vibrations, attributed to surface hydroxyl groups or adsorbed water, while at 1632 cm^{-1}, the peak could be assigned to H–O–H bending vibrations of adsorbed water or surface hydroxyls. The band around 1362 cm^{-1} can be attributed to the CO_3^{2-} vibration mode [51]. Additionally, the 781 cm^{-1} peak corresponds to Al–O vibration modes, characteristic of the Al_2O_3 support structures [52].

Upon catalytic upgrading via hydrodeoxygenation (HDO) of guaiacol, the spent catalyst exhibited significant spectral changes. New peaks appear at 1067 cm^{-1}, 1396 cm^{-1}, 1549 cm^{-1}, and 1627 cm^{-1}, indicating surface deposition of reaction intermediates or by-products. The 1067 cm^{-1} peak is attributed to C–O stretching from residual oxygenated organic species, such as alcohols or phenolics. The 1396 cm^{-1} peak corresponds to C–H bending vibrations from aliphatic hydrocarbons formed during hydrogenation. Peak at 1549 cm^{-1} is known as the coke band, and at 1627 cm^{-1} suggests aromatic C=C stretching, indicating incomplete deoxygenation of guaiacol's aromatic ring. Peaks at 2926 cm^{-1} could be attributed to C-H stretching vibration in CH_n aliphatic groups. Additionally, a broad peak at 3380 cm^{-1} was observed in the spent catalyst, likely due to an increase in surface hydroxyl groups or adsorbed water, potentially formed as a by-product during the HDO process [53,54]. Therefore, these FTIR confirmed some transformation in the catalyst surface chemistry due to the adsorption of organic compounds. Other catalyst cleaning methodologies or reactivation methods should be developed.

4. Conclusions

The composition of the layered double hydroxides from which Ni and NiCu catalysts were prepared were determinant for the selective obtention of cyclohexane and cyclohexanol under the reaction conditions used. Thus, the catalysts obtained from Ni/Al and Ni/Cu/Al hydrotalcites were more selective to cyclohexane due to their higher metallic content, higher metallic area, and very low basicity. The obtention of cyclohexane with catalysts prepared from hydrotalcite-like materials for this reaction is remarkable since it has not been reported before. This could mainly related to the reaction conditions used (300 °C, 50 bar H_2). However, the magnesium species present in the catalysts obtained from Ni/Mg/Al and Ni/Cu/Mg/Al hydrotalcites, affected their catalytic activity making them more selective to cyclohexanol. This was related to the lower metallic content, lower metallic area, and higher basicity of these catalysts. The higher content of Ni or Cu in the NiCu alloy formed in the bimetallic catalysts affected the selectivity to cyclohexane or cyclohexanol. When combined with H-βeta, the Brønsted acidity provided by the zeolite, due to the parallel transformation of the solvent used, dodecane, under the reaction conditions, led to an overproduction of cyclohexane. On the other hand, the addition of small amounts of Lewis acidity (ReOx) to the catalysts obtained from Ni/Al and NiCu/Al hydrotalcites favoured the formation of cyclohexanol due to the difficulty in the reduction of the catalytic precursors to Ni, favoring the binding of the oxygenated compounds.

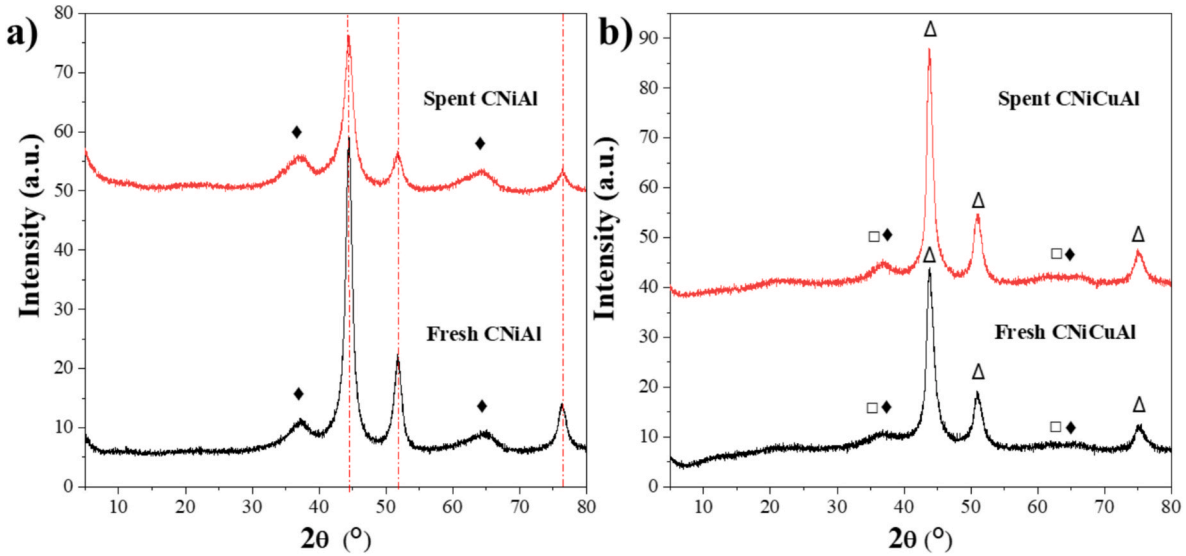

Fig. 14. XRD patterns of the fresh and spent a) CNiAl and b) NiCuAl catalysts. Crystalline phases: (◆) NiO, (-·-) Ni, (□) Cu_2O, (Δ) NiCu alloy,

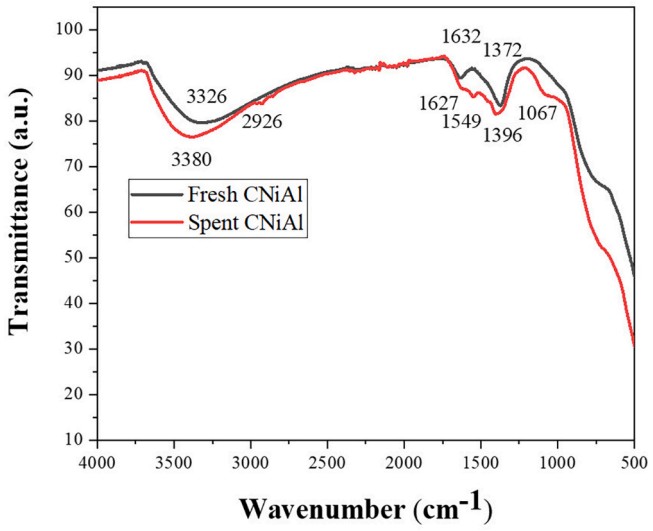

Fig. 15. FTIR spectra of fresh and spent NiAl catalyst.

CRediT authorship contribution statement

Angie C. Rueda: Writing – original draft, Methodology, Investigation, Conceptualization. **Judith Granados-Reyes:** Validation, Supervision, Conceptualization. **Julien Delaunay:** Methodology, Investigation. **Pau Mora-Masià:** Methodology, Investigation. **Yolanda Cesteros:** Writing – review & editing, Writing – original draft, Validation, Supervision, Resources, Methodology, Funding acquisition, Conceptualization.

Declaration of competing interest

The authors declare that they have no known competing financial interests or personal relationships that could have appeared to influence the work reported in this paper.

Acknowledgments

This work was supported by the project PID2019-110735RB-C22 funded by MICIU/AEI/ 10.13039/501100011033. A. Rueda thanks to Generalitat de Catalunya for the FI_B 00128 grant. XPS results were performed at SRCiT (URV) using a ProvenX-NAP system, totally funded by Ministerio de Ciencia e Innovación and European Union "Next Generation", project EQC2021-007785-P). We acknowledge Francesc Gispert Guirado for his help in the treatment of the XRD results.

Appendix A. Supplementary data

Supplementary data to this article can be found online at https://doi.org/10.1016/j.cej.2025.162226.

Data availability

The data that has been used is confidential.

References

[1] Energy Institute. 2024 Statistical Review of World Energy, 73rd Eidition (2024). https://www.energyinst.org/statistical-review.
[2] European Commission, The EU Green Deal – a roadmap to sustainable economies, (2019).
[3] European Commission, Renewable energy targets, Renew. Energy Targets (2023). https://energy.ec.europa.eu/topics/renewable-energy/renewable-energy-directive-targets-and-rules/renewable-energy-targets_en#:~:text=The 2030 targets,-Building on the&text=The Commission presented Europe's new,overall energy mix by 2030.
[4] V. Ashokkumar, R. Venkatkarthick, S. Jayashree, S. Chuetor, S. Dharmaraj, G. Kumar, W.-H. Chen, C. Ngamcharussrivichai, Recent advances in lignocellulosic biomass for biofuels and value-added bioproducts - A critical review, Bioresour. Technol. 344 (2022) 126195, https://doi.org/10.1016/j.biortech.2021.126195.
[5] H. Wang, Y. Pu, A. Ragauskas, B. Yang, From lignin to valuable products–strategies, challenges, and prospects, Bioresour. Technol. 271 (2019) 449–461, https://doi.org/10.1016/j.biortech.2018.09.072.
[6] P. He, L. Li, Y. Shao, Q. Yi, Z. Liu, H. Geng, Y. Liu, V. Valtchev, Recent advances in hydrodeoxygenation of lignin-derived phenolics over metal-zeolite bifunctional catalysts, ChemCatChem 16 (2024), https://doi.org/10.1002/cctc.202301681.
[7] J.G. Tillou, C.J. Ezeorah, J.J. Kuchta, S.C.D. Dissanayake Mudiyanselage, J. D. Sitter, A.K. Vannucci, A review on recent trends in selective hydrodeoxygenation of lignin derived molecules, RSC Sustain. 1 (2023) 1608–1633, https://doi.org/10.1039/D3SU00232B.
[8] H. Wang, H. Ruan, M. Feng, Y. Qin, H. Job, L. Luo, C. Wang, M.H. Engelhard, E. Kuhn, X. Chen, M.P. Tucker, B. Yang, One-pot process for hydrodeoxygenation of lignin to alkanes using Ru-based bimetallic and bifunctional catalysts supported on zeolite Y, ChemSusChem 10 (2017) 1846–1856, https://doi.org/10.1002/cssc.201700160.
[9] J. Kong, B. Li, C. Zhao, Tuning Ni nanoparticles and the acid sites of silica-alumina for liquefaction and hydrodeoxygenation of lignin to cyclic alkanes, RSC Adv. 6 (2016) 71940–71951, https://doi.org/10.1039/C6RA16977E.
[10] E. Blanco, A.B. Dongil, N. Escalona, Synergy between Ni and Co nanoparticles supported on carbon in guaiacol conversion, Nanomaterials 10 (2020) 2199, https://doi.org/10.3390/nano10112199.
[11] I.T. Ghampson, C. Sepúlveda, R. Garcia, B.G. Frederick, M.C. Wheeler, N. Escalona, W.J. DeSisto, Guaiacol transformation over unsupported molybdenum-based nitride catalysts, Appl. Catal. A Gen. 413–414 (2012) 78–84, https://doi.org/10.1016/j.apcata.2011.10.050.
[12] S. Gutiérrez-Rubio, I. Moreno, D.P. Serrano, J.M. Coronado, Hydrotreating of guaiacol and acetic acid blends over Ni 2 P/ZSM-5 catalysts: elucidating molecular interactions during bio-oil upgrading, ACS Omega 4 (2019) 21516–21528, https://doi.org/10.1021/acsomega.9b03221.
[13] K. Leiva, R. Garcia, C. Sepulveda, D. Laurenti, C. Geantet, M. Vrinat, J.L. Garcia-Fierro, N. Escalona, Conversion of guaiacol over supported ReOx catalysts: Support and metal loading effect, Catal. Today 296 (2017) 228–238, https://doi.org/10.1016/j.cattod.2017.04.002.
[14] H. Lee, H. Kim, M.J. Yu, C.H. Ko, J.-K. Jeon, J. Jae, S.H. Park, S.-C. Jung, Y.-K. Park, Catalytic hydrodeoxygenation of bio-oil model compounds over Pt/HY catalyst, Sci. Rep. 6 (2016) 28765, https://doi.org/10.1038/srep28765.
[15] R. Shu, Z. Zhong, H. You, Z. Tian, Y. Chen, L. Ma, Hydrodeoxygenation of lignin-derived phenolic compounds over Ru/TiO_2–CeO_2 catalyst prepared by photochemical reduction method, J. Energy Inst. 99 (2021) 1–8, https://doi.org/10.1016/j.joei.2021.07.012.
[16] J. Matos, D. Samudio-González, E. Blanco, P.S. Poon, N. Escalona, Alkali-driven selectivity of products on carbon-supported Ni-based catalysts during the HDO of guaiacol, Fuel 374 (2024) 132442, https://doi.org/10.1016/j.fuel.2024.132442.
[17] Y. Liu, X. Zhang, L. Chen, J. Liu, Q. Zhang, L. Ma, A Cu-ZnO-Al2O3 catalyst with oxygen vacancy for efficient hydrodeoxygenation of lignin-derived guaiacol to hydrocarbons, Chem. Eng. Sci. 285 (2024) 119616, https://doi.org/10.1016/j.ces.2023.119616.
[18] M. Saidi, F. Samimi, D. Karimipourfard, T. Nimmanwudipong, B.C. Gates, M. R. Rahimpour, Upgrading of lignin-derived bio-oils by catalytic hydrodeoxygenation, Energy Environ. Sci. 7 (2014) 103–129, https://doi.org/10.1039/C3EE43081B.
[19] K. Leiva, N. Martinez, C. Sepulveda, R. García, C.A. Jiménez, D. Laurenti, M. Vrinat, C. Geantet, J.L.G. Fierro, I.T. Ghampson, N. Escalona, Hydrodeoxygenation of 2-methoxyphenol over different Re active phases supported on SiO 2 catalysts, Appl. Catal. A Gen. 490 (2015) 71–79, https://doi.org/10.1016/j.apcata.2014.10.054.
[20] E. Blanco, A.B. Dongil, J.L. García-Fierro, N. Escalona, Insights in supported rhenium carbide catalysts for hydroconversion of lignin-derived compounds, Appl. Catal. A Gen. 599 (2020) 117600, https://doi.org/10.1016/j.apcata.2020.117600.
[21] M.V. Bykova, D.Y. Ermakov, V.V. Kaichev, O.A. Bulavchenko, A.A. Saraev, M. Y. Lebedev, V. Yakovlev, Ni-based sol–gel catalysts as promising systems for crude bio-oil upgrading: Guaiacol hydrodeoxygenation study, Appl. Catal. B Environ. 113–114 (2012) 296–307, https://doi.org/10.1016/J.APCATB.2011.11.051.
[22] Z. Tian, X. Liang, R. Li, C. Wang, J. Liu, L. Lei, R. Shu, Y. Chen, Hydrodeoxygenation of guaiacol as a model compound of pyrolysis lignin-oil over NiCo bimetallic catalyst: Reactivity and kinetic study, Fuel 308 (2022) 122034, https://doi.org/10.1016/j.fuel.2021.122034.
[23] C.R. Lee, J.S. Yoon, Y.-W. Suh, J.-W. Choi, J.-M. Ha, D.J. Suh, Y.-K. Park, Catalytic roles of metals and supports on hydrodeoxygenation of lignin monomer guaiacol, Catal. Commun. 17 (2012) 54–58, https://doi.org/10.1016/j.catcom.2011.10.011.
[24] J. Chang, T. Danuthai, S. Dewiyanti, C. Wang, A. Borgna, Hydrodeoxygenation of Guaiacol over Carbon-Supported Metal Catalysts, ChemCatChem 5 (2013) 3041–3049, https://doi.org/10.1002/cctc.201300096.
[25] E.H. Lee, R. Park, H. Kim, S.H. Park, S.-C. Jung, J.-K. Jeon, S.C. Kim, Y.-K. Park, Hydrodeoxygenation of guaiacol over Pt loaded zeolitic materials, J. Ind. Eng. Chem. 37 (2016) 18–21, https://doi.org/10.1016/j.jiec.2016.03.019.
[26] O. Bergadà, P. Salagre, Y. Cesteros, F. Medina, J.E. Sueiras, Effective catalysts, prepared from several hydrotalcites aged with and without microwaves, for the clean obtention of 2-phenylethanol, Appl. Catal. A Gen. 331 (2007) 19–25, https://doi.org/10.1016/J.APCATA.2007.07.017.

[27] J. Wu, G. Gao, J. Li, P. Sun, X. Long, F. Li, Efficient and versatile CuNi alloy nanocatalysts for the highly selective hydrogenation of furfural, Appl. Catal. B Environ. 203 (2017) 227–236, https://doi.org/10.1016/J.APCATB.2016.10.038.
[28] Z. Wang, W. Zhang, C. Li, C. Zhang, Recent Progress of Hydrogenation and Hydrogenolysis Catalysts Derived from Layered Double Hydroxides, Catalysts 12 (2022) 1484, https://doi.org/10.3390/catal12111484.
[29] D. Guo, B. Cai, R. Kang, S. Wang, J. Feng, H. Pan, Selective hydrodeoxygenation of guaiacol to cyclohexanol over NixCoyAlz catalysts under mild conditions, J. Anal. Appl. Pyrolysis 170 (2023) 105876, https://doi.org/10.1016/j.jaap.2023.105876.
[30] L. Huang, F. Tang, P. Liu, W. Xiong, S. Jia, F. Hao, Y. Lv, H. Luo, Highly efficient and selective conversion of guaiacol to cyclohexanol over Ni-Fe/MgAlOx: Understanding the synergistic effect between Ni-Fe alloy and basic sites, Fuel 327 (2022) 125115, https://doi.org/10.1016/j.fuel.2022.125115.
[31] Z. Wang, A. Wang, L. Yang, G. Fan, F. Li, Supported Ru nanocatalyst over phosphotungstate intercalated Zn-Al layered double hydroxide derived mixed metal oxides for efficient hydrodeoxygenation of guaiacol, Mol. Catal. 528 (2022) 112503, https://doi.org/10.1016/j.mcat.2022.112503.
[32] W. Perez, J. Marín, U. Arnold, L. Rios, Conversion of lignocellulosic waste into cyclohexanol and 1-methyl-1,2- cyclohexanediol using new hydrotalcite-based, Catalysts (2023), https://doi.org/10.21203/rs.3.rs-2917757/v1.
[33] P. Ciambelli, D. Sannino, V. Palma, V. Vaiano, Photocatalysed selective oxidation of cyclohexane to benzene on MoOx/TiO2, Catal. Today 99 (2005) 143–149, https://doi.org/10.1016/j.cattod.2004.09.034.
[34] S. Rao, Z. Zheng, C. Yang, Effect of cyclohexane on the combustion characteristics of multi-component gasoline surrogate fuels, Molecules 28 (2023) 4273, https://doi.org/10.3390/molecules28114273.
[35] Z. Zhang, M. Hu, Q. Gui, J. Gu, W. Xu, Q. Xiao, W. Huang, Highly enhanced direct catalytic oxidation of cyclohexane to adipic acid with molecular oxygen: Dynamic collaboration between zeolite channel micro-environment and Au clusters, Chem. Eng. J. 467 (2023) 143501, https://doi.org/10.1016/j.cej.2023.143501.
[36] M. Ghiaci, S.M. Hosseini, A. Shahzeydi, M.V. Martínez-Huerta, Oxidation of cyclohexanol to adipic acid with molecular oxygen catalyzed by ZnO nanoparticles immobilized on hydroxyapatite, RSC Adv. 6 (2016) 78487–78495, https://doi.org/10.1039/C6RA12831A.
[37] R. Wang, Y. Kang, J. Wu, T. Jiang, Y. Wang, L. Gu, Y. Li, X. Yang, Z. Liu, M. Gong, Electrifying adipic acid production: copper-promoted oxidation and C−C Cleavage of cyclohexanol, Angew. Chemie 134 (2022), https://doi.org/10.1002/ange.202214977.
[38] J. Rios, J. Lebeau, T. Yang, S. Li, M.D. Lynch, A critical review on the progress and challenges to a more sustainable, cost competitive synthesis of adipic acid, Green Chem. 23 (2021) 3172–3190, https://doi.org/10.1039/D1GC00638J.
[39] D. Balzar, Voigt-function model in diffraction line-broadening analysis, Int. Union Crystallogr. Monogr. Crystallogr. 10 (2000).
[40] A.R. Stokes, A.J.C. Wilson, A method of calculating the integral breadths of Debye-Scherrer lines: generalization to non-cubic crystals, Math. Proc. Cambridge Philos. Soc. 40 (1944) 197–198, https://doi.org/10.1017/S0305004100018314.
[41] X. Yu, F. Zhang, W. Chu, Effect of a second metal (Co, Cu, Mn or Zr) on nickel catalysts derived from hydrotalcites for the carbon dioxide reforming of methane, RSC Adv. 6 (2016) 70537–70546, https://doi.org/10.1039/C6RA12335J.
[42] J. Granados-Reyes, A.C. Rueda, Y. Cesteros, Synthesis of NiCuMgAl-layered double hydroxides using advanced microwave and ultrasound methods, Appl. Clay Sci. 261 (2024) 107590, https://doi.org/10.1016/j.clay.2024.107590.
[43] D. Gupta, R. Kumar, K.K. Pant, Hydrotalcite supported bimetallic (Ni-Cu) catalyst: A smart choice for one-pot conversion of biomass-derived platform chemicals to hydrogenated biofuels, Fuel 277 (2020) 118111, https://doi.org/10.1016/j.fuel.2020.118111.
[44] J. Ashok, M. Subrahmanyam, A. Venugopal, Hydrotalcite structure derived Ni–Cu–Al catalysts for the production of H_2 by CH_4 decomposition, Int. J. Hydrogen Energy 33 (2008) 2704–2713, https://doi.org/10.1016/j.ijhydene.2008.03.028.
[45] C. Miao, G. Zhou, S. Chen, H. Xie, X. Zhang, Synergistic effects between Cu and Ni species in NiCu/γ-Al_2O_3 catalysts for hydrodeoxygenation of methyl laurate, Renew. Energy 153 (2020) 1439–1454, https://doi.org/10.1016/j.renene.2020.02.099.
[46] D. Li, M. Koike, J. Chen, Y. Nakagawa, K. Tomishige, Preparation of Ni–Cu/Mg/Al catalysts from hydrotalcite-like compounds for hydrogen production by steam reforming of biomass tar, Int. J. Hydrogen Energy 39 (2014) 10959–10970, https://doi.org/10.1016/j.ijhydene.2014.05.062.
[47] M. Lu, Y. Sun, P. Zhang, J. Zhu, M. Li, Y. Shan, J. Shen, C. Song, Hydrodeoxygenation of guaiacol catalyzed by high-loading Ni catalysts supported on SiO_2 –TiO_2 binary oxides, Ind. Eng. Chem. Res. 58 (2019) 1513–1524, https://doi.org/10.1021/acs.iecr.8b04517.
[48] A.B. Dongil, B. Bachiller-Baeza, I. Rodríguez-Ramos, J.L.G. Fierro, N. Escalona, The effect of Cu loading on Ni/carbon nanotubes catalysts for hydrodeoxygenation of guaiacol, RSC Adv. 6 (2016) 26658–26667, https://doi.org/10.1039/C6RA00041J.
[49] X. Wang, S. Zhu, S. Wang, Y. He, Y. Liu, J. Wang, W. Fan, Y. Lv, Low temperature hydrodeoxygenation of guaiacol into cyclohexane over Ni/SiO_2 catalyst combined with Hβ zeolite, RSC Adv. 9 (2019) 3868–3876, https://doi.org/10.1039/C8RA09972C.
[50] A. Casadó, A. Rösch, A.C. Rueda, A. Uribe, M.D. González, A.J. Romero, J. J. Carvajal, Y. Cesteros, Catalytic potential of green ordered mesoporous carbons, obtained from biomass-derived xylose, glucose, and lignin, Microporous Mesoporous Mater. 372 (2024) 113097, https://doi.org/10.1016/j.micromeso.2024.113097.
[51] X. Kong, R. Zheng, Y. Zhu, G. Ding, Y. Zhu, Y.-W. Li, Rational design of Ni-based catalysts derived from hydrotalcite for selective hydrogenation of 5-hydroxymethylfurfural, Green Chem. 17 (2015) 2504–2514, https://doi.org/10.1039/C5GC00062A.
[52] K.V. Manukyan, A.J. Cross, A.V. Yeghishyan, S. Rouvimov, J.J. Miller, A. S. Mukasyan, E.E. Wolf, Highly stable Ni–Al_2O_3 catalyst prepared from a Ni–Al layered double hydroxide for ethanol decomposition toward hydrogen, Appl. Catal. A Gen. 508 (2015) 37–44, https://doi.org/10.1016/j.apcata.2015.10.007.
[53] E. Fernandez, L. Santamaria, I. García, M. Amutio, M. Artetxe, G. Lopez, J. Bilbao, M. Olazar, Elucidating coke formation and evolution in the catalytic steam reforming of biomass pyrolysis volatiles at different fixed bed locations, Chin. J. Catal. 48 (2023) 101–116, https://doi.org/10.1016/S1872-2067(23)64407-9.
[54] J.V. Ibarra, C. Royo, A. Monzón, J. Santamaría, Fourier transform infrared spectroscopic study of coke deposits on a Cr_2O_3-Al_2O_3 catalyst, Vib. Spectrosc. 9 (1995) 191–196, https://doi.org/10.1016/0924-2031(95)00005-F.